Structure-function based study on the logarithmic region in atmospheric surface layer with and without sand

Fei-Chi Zhang [1] Jin-Han Xie [1,2,*] and Xiaojing Zheng [1,3,†]

[1] *Department of Mechanics and Engineering Science at College of Engineering, and State Key Laboratory for Turbulence and Complex Systems, Peking University, Beijing 100871, People's Republic of China*

[2] *Joint Laboratory of Marine Hydrodynamics and Ocean Engineering, Pilot National Laboratory for Marine Science and Technology (Qingdao), Shandong 266237, People's Republic of China*

[3] *Center for Particle-Laden Turbulence, Lanzhou University, Lanzhou 730000, People's Republic of China*

(Received 11 May 2022; accepted 9 August 2022; published 24 August 2022)

In the logarithmic layer of boundary-layer turbulence, velocity structure functions scale as power and logarithmic functions of displacement at small and large scales, respectively. The small-scale scaling can be explained as a near-isotropy behavior, while the mechanism behind the logarithmic behavior is debatable. By rescaling the horizontal displacement by the distance to the wall, using the attached eddy hypothesis to the Kármán-Howarth-Monin (KHM) equation results in the logarithmic behavior. Also, from the picture of energy cascade, i.e., introducing a characteristic scale u_τ^3/ϵ with u_τ and ϵ the friction velocity and energy dissipation rate, respectively, the logarithmic profile of the third-order structure function can also be obtained. These two explanations suggest a dependence of the third-order structure function on the difference between local production and dissipation. By analyzing data measured from the Qingtu Lake Observation Array built on a dry flatbed of Qingtu Lake in Minqin (China) with $\mathrm{Re}_\tau = O(10^6)$, we provide evidence for the scaling behaviors and justify the underlying balances in the range with large displacements. And we study the robustness of the structure function theory using clear-air and sand-containing data: sands modify key statistical quantities of the boundary-layer turbulence, such as the height dependence of the Reynolds stress, but the behavior of the third-order structure function remains unchanged. Considering that the shear production captures the strength of anisotropic perturbation-mean interaction in the KHM equation, the ratio of production and dissipation controls the relative extensions of the power and logarithmic ranges, and a stronger production leads to a relatively wider logarithmic range, which is justified by measured data.

DOI: 10.1103/PhysRevFluids.7.084609

I. INTRODUCTION

In the logarithmic region of boundary-layer turbulence, the velocity statistics always show logarithmic dependence on spatial variables, a celebrated example of which is the mean flow log law:

$$U^+ = \frac{1}{\kappa}\ln z^+ + B, \tag{1}$$

*jinhanxie@pku.edu.cn
†xjzheng@lzu.edu.cn

where U^+ is streamwise mean velocity U normalized by the friction velocity $u_\tau = \sqrt{\tau_w/\rho}$ with τ_w the shear stress at the wall and ρ the flow density [1], z is the distance to the boundary and $z^+ = zu_\tau/\nu$ with ν the kinematic viscosity, κ is the von Kármán constant, and B is a constant depending on flow conditions. Proven in many approaches [2–4] and confirmed by experiments and numerical simulations [5–7], the logarithmic form of streamwise mean velocity is important for engineering applications, as it appears in many numerical models [8].

Besides, higher-order statistical properties of velocity also show logarithmic forms, such as the moments of fluctuating velocity [4,9–11]. This paper focuses on the two-point structure functions. Defined as the moments of velocity increment, the structure functions are successfully used to understand the statistics of turbulence and to detect energy transfer across scales [12–15]. In the logarithmic layer of boundary-layer turbulent flows, the logarithmic scalings of structure functions have been explored for decades. Under the assumption of Townsend's attached eddy hypothesis (AEH) [4], in the logarithmic region, the characteristic eddies are self-similar and scale with the distance to the wall z [16]. Davidson *et al.* [17] proposed that, for the eddy whose scale characterized by the streamwise distance of two measured points r is greater than the distance z from the wall, the kinetic energy density can be estimated as $d\langle\Delta u^2\rangle/dr$, where Δu is the streamwise velocity increment and the angular brackets denote the ensemble average. And for eddies of size r, their total kinetic energy is approximately on the order of u_τ^2, i.e., $rd\langle\Delta u^2\rangle/dr \sim u_\tau^2$. Therefore, using the length scale z to normalize r, the second-order longitudinal structure function shows logarithmic dependence of r/z:

$$\langle\Delta u^{+2}\rangle = C_2 + B_2 \ln\left(\frac{r}{z}\right), \tag{2}$$

where Δu^+ is the streamwise velocity increment normalized by u_τ, and C_2 and B_2 are constants. This logarithmic behavior in r space corresponds to the k^{-1} spectrum of streamwise velocity, where k is the streamwise wave number. Unlike the k^{-1} law, which is difficult to see in spectra, the $\ln r$ law is more conspicuous in the second-order structure function, which was supported by experimental evidence [18–21]. Later, Davidson *et al.* [18] discovered that the constant B_2 should be a universal constant, while C_2 shows logarithmic dependence on the ratio of the local energy production rate P and dissipation rate ϵ, which indicates the importance of energy flux in the turbulence structure of the logarithmic layer. Davidson and Krogstad [19] further argued that the $\ln(r/z)$ law could be achieved without the aid of the AEH.

Since P/ϵ is z dependent in most turbulent shear layers, Davidson and Krogstad [10] proposed that the combination r/z may not be appropriate. They put forward that, differing from the characteristic scale z based on AEH, the characteristic length scale should be u_τ^3/ϵ and therefore the second-order structure-function relation becomes

$$\langle\Delta u^{+2}\rangle = A_2 - B_2 \ln\left(\frac{\kappa P}{\epsilon}\right) + B_2 \ln\left(\frac{r}{z}\right) = A_2 + B_2 \ln\left(\frac{\epsilon r}{u_\tau^3}\right), \tag{3}$$

where A_2 and B_2 are universal constants for smooth-wall boundary layers. By analyzing experimental data this scaling is justified to be universal with different distances to the wall for both smooth- and rough-wall boundary-layer turbulence. They argued that z is an important scale only to the extent that z sets the value of the dissipation rate ϵ and the turbulence structure is actually controlled by ϵ. Moreover, analogous to the derivation of the mean velocity log law, they asymptotically matched the expressions of $rd\langle\Delta u^2\rangle/dr$ close to the wall and at the bulk to obtain the logarithmic expression of $\langle\Delta u^{+2}\rangle$. Though the structure functions are more convergent using $\epsilon r/u_\tau^3$ scaling compared with r/z, the constants in the expression for the logarithmic regime of second-order structure function are not determined, which is nonuniversal for smooth- and rough-wall boundary layers.

de Silva *et al.* [20] studied the scaling of streamwise even-order structure functions up to 10th order and justified the logarithmic behavior of $\langle\Delta u^2\rangle$ with respect to r/z using experimental data from the University of Melbourne. Using a different derivation procedure from Davidson *et al.* [17], the logarithmic behavior of structure functions is obtained and further explored by

Yang *et al.* [22] based on AEH. Xie *et al.* [21] checked the consistency between AEH and the Kármán-Howarth-Monin (KHM) equation in the logarithmic regime of the third-order structure function. Under the assumption of small-scale isotropy and local production-dissipation balance, by matching the inertial and logarithmic regimes of the third-order structure function, their theory provides an expression for the third-order structure function that involves the von Kármán constant κ as the only parameter.

Since the above theories for boundary-layer turbulence are developed for situations with large Reynolds numbers, data from measurements in the atmospheric surface layer (ASL) is invaluable for its high Reynolds number that cannot be achieved in either numerical simulations or experiments. Defined as the lower part of the atmospheric boundary layer, ASL flow can achieve high friction Reynolds number up to the order of $O(10^6)$. Also, multipoint three-dimensional velocity data can be measured from ASL, e.g., the Surface Layer Turbulence and Environmental Science Test [23,24] and the Qingtu Lake Observation Array (QLOA) [25], and one can study spatial structure functions based on Taylor's frozen hypothesis [26].

In some extreme weather conditions, ASL flows contain sand and dust particles that rise from the ground or are carried along from afar to form sandstorms. As complicated gas-sand two-phase flows associated with extremely high Reynolds numbers, sandstorm lacks a theoretical description of its turbulent structures and mechanical process due to the complicated interaction between the two phases and the difficulty of observation. In particle-laden turbulent flows, the effect of particles induces turbulence modulation [27–30], such as the enhancement or suppression of turbulence intensity and the distribution of mean velocity affected by particles with different diameters [31,32], the interaction between sand particles and very-large-scale motions in-field measurements and numerical simulation of ASL [33–36], etc. As for the logarithmic region in sediment-laden flow, the validity of the log law for mean flow has been examined, while the von Kármán constant κ is disputed for decreasing with sediment suspension [37–41] or maintaining a universal value of approximately 0.41 [42–46]. Besides, the study of structure-function scalings is lacking in particle-laden flow, especially in ASL sandstorms.

Very large scale structures exist in ASL turbulence, and they may be controlled by external factors [24,25,47]. Thus, to explore the universal behavior of boundary layers, we focus on the third-order structure function with scales much smaller than the boundary thickness δ. Using high-quality ASL data measured at QLOA, we check some basic assumptions in the theory of third-order structure function in boundary-layer turbulence, such as the small-scale Kolmogorov four-fifths law and the balances of the KHM equation at the logarithmic region. Inspired by Davidson and Krogstad [10]'s introduction of the combination of ϵ and u_τ as a length scale, this paper proposes that we may use the combination of ϵ and z, instead of u_τ, to scale the velocity to obtain the expression of third-order structure function [cf. Eq. (17)], which is one of our main results. And we derive extensions to the theory of Xie *et al.* [21] to achieve our two main aims: (i) justifying the theory of third-order structure function with data at $\mathrm{Re}_\tau = O(10^6)$ and (ii) exploring the universal behavior of matching the power and logarithmic regimes of third-order structure function at a specific transition scale.

The rest of this paper is organized as follows. We provide the theoretical expressions for the third-order structure function in boundary-layer turbulence in Sec. II. The detail of data measurements is demonstrated in Sec. III. In Sec. IV we justify the theoretical results using measured data and explore the dependence of the third-order structure function on the difference between local production and dissipation. We summarize and discuss our results in Sec. V. The differences between our expression and other alternative choices are discussed in the Appendix.

II. THEORY FOR THE THIRD-ORDER STRUCTURE FUNCTION IN THE LOGARITHMIC REGION

Enlightened by AEH, Davidson *et al.* [17], de Silva *et al.* [20], and Xie *et al.* [21] chose z as the characteristic spatial scale for the second- and third-order structure function, while Davidson and Krogstad [10] argued that, different from AEH, turbulent structures are controlled by the energy flux; therefore, the characteristic spatial scale should be u_τ^3/ϵ. Thus we have two characteristic length scales, z and u_τ^3/ϵ, and therefore, based on dimensional analysis, we obtain the expression for the third-order structure function

$$\langle \Delta u^{+3}\rangle = \tilde{\phi}\left(\frac{r}{z}, \frac{u_\tau^3}{z\epsilon}\right) = \phi\left(\frac{r}{z}, \frac{P}{\epsilon}\right), \tag{4}$$

where $\tilde{\phi}$ and ϕ are functions to be determined. Here, $P = -\langle uw\rangle U_z \approx u_\tau^3/(\kappa z)$ is the local production with U_z the derivative of U with respect to z, and the logarithmic behavior of the mean flow is used in the second equality. In canonical boundary layer turbulence, de Silva *et al.* [20] and Xie *et al.* [21] claimed that

$$\langle \Delta u^{+3}\rangle = \tilde{\phi}_1\left(\frac{r}{z}\right), \tag{5}$$

where the local equality of energy production and dissipation is assumed, while Davidson and Krogstad [10] proposed that

$$\langle \Delta u^{+3}\rangle = \tilde{\phi}_2\left(\frac{\epsilon r}{u_\tau^3}\right). \tag{6}$$

The difference between Eqs. (5) and (6) is that the former considers situations with local production-dissipation balance [48], i.e., $P/\epsilon \approx 1$, while the latter applies to situations with z-dependent P/ϵ.

Considering the underlying energy-flux picture, we can choose a characteristic velocity different from u_τ to nondimensionalize the third-order structure function, i.e., a combination of ϵ and z; thus we obtain two other expressions:

$$\frac{\langle \Delta u^3\rangle}{\epsilon z} = \tilde{\phi}_3\left(\frac{r}{z}\right) \tag{7}$$

and

$$\frac{\langle \Delta u^3\rangle}{\epsilon z} = \tilde{\phi}_4\left(\frac{\epsilon r}{u_\tau^3}\right). \tag{8}$$

Noting that Eq. (7) is independent of u_τ, whose value is not easily measured directly [25,49], it may be a better candidate for analyzing ASL data. Also, Eqs. (7) and (8) are special cases of Eq. (4).

Before we propose the third-order structure function expressions used in analyzing measured data, we briefly review the derivation of logarithmic function from the KHM equation in Xie *et al.* [21], where the key steps were not possible to be justified using low Reynolds number data. Now we justify them in Sec. IV B using ASL data with high friction Reynolds number.

A. Derivation of the logarithmic behavior of structure functions from the KHM equation

In this section, we review the third-order structure-function theory proposed by Xie *et al.* [21]. The key idea of their theory is matching the small-scale Kolmogorov's expression and the large-scale logarithmic expression based on AEH. At small scale, Kolmogorov's theory [12] leads to

$$\langle \Delta u^3\rangle = -\tfrac{4}{5}\epsilon r, \quad r_\nu \ll r < r_m, \tag{9}$$

where r_ν and r_m denote Kolmogorov's microscale and the transition scale between the inertial subrange and the logarithmic range.

Based on AEH and considering that the two measured points have the same distance to the wall, the logarithmic expression of $\langle \Delta u^3\rangle$ is obtained as

$$\langle \Delta u^3\rangle = D_3^* \ln(r/z) + B_3^*, \quad r_m < r \ll \delta, \tag{10}$$

where D_3^* and B_3^* are constants and δ is the boundary layer thickness. Equation (10) is also obtained from the KHM equation. Starting from the Navier-Stokes equation for the fully developed statistically steady state, the transport equation for the second-order structure function is reduced to

$$\frac{\partial\langle|\Delta\mathbf{u}|^2\Delta u\rangle}{\partial r'} - r'\frac{\partial\langle|\Delta\mathbf{u}|^2 w_c\rangle}{\partial r'} = 2\langle u_1 w_2 + w_1 u_2\rangle\frac{u_\tau}{\kappa}, \tag{11}$$

where $\mathbf{u} = (u, v, w)$ is the instantaneous fluctuating velocity vector with u, v, and w the streamwise, spanwise, and vertical velocity fluctuations, respectively, the subscripts 1 and 2 represent point 1 at $x_1 = x$ and point 2 at $x_2 = x + r$, $w_c = (w_1 + w_2)/2$, and $r' = r/z$ for simplicity. For intermediate scale, i.e., $r_m/z < r' \ll \delta/z$,

$$\langle u_1 w_2 + w_1 u_2\rangle \sim \frac{1}{r'}, \quad \langle|\Delta\mathbf{u}|^2 w_c\rangle \sim \frac{1}{r'}. \tag{12}$$

Thus integrating Eq. (11) yields the logarithmic expression Eq. (10).

To explore a universal behavior, we can normalize velocities using the friction velocity u_τ. Since the surface stress is not directly obtained in the ASL measurement, practically, when z is located at the logarithmic layer, one can introduce the estimation $u_\tau^2 = \nu(dU/dz)|_{z=0} \approx -\langle uw\rangle$, where u and w are streamwise and vertical fluctuating velocity, respectively, and $\langle uw\rangle$ is the Reynolds stress and is also the vertical momentum flux. Under the assumption of local balance between shear production and dissipation [1,50], i.e., $\epsilon \approx P = -\langle uw\rangle dU/dz \approx u_\tau^3/(\kappa z)$, Eqs. (9) and (10) become

$$\langle\Delta u^{+3}\rangle = -\frac{4}{5\kappa}\frac{r}{z}, \quad r_\nu \ll r < r_m, \tag{13a}$$

$$\langle\Delta u^{+3}\rangle = D_3 \ln\left(\frac{r}{z}\right) + B_3, \quad r_m < r \ll \delta, \tag{13b}$$

where D_3 is a universal constant and B_3 is a flow-dependent constant [20].

The common form of dependent variables, r/z, implies a possible direct matching between Eqs. (13a) and (13b). Under the assumption that there is no distinguished regime between the Kolmogorov and logarithmic regimes, by matching at $r/z = 1$ ($r_m = z$; cf. [19]), Xie *et al.* [21] obtained $D_3 = B_3 = -4/(5\kappa)$. Therefore, with the von Kármán constant $\kappa \approx 0.4$, the constants in Eq. (13b) are determined as $D_3 = B_3 = -2$, which is close to the fitted values from data. In our data analysis, we find that this expression does not well capture the statistics of ASL data, so in the next section we propose new expressions and use them to explore the properties of ASL turbulence.

B. Alternative expressions for the third-order structure function

Under the assumption of Kolmogorov's phenomenology Eq. (9) at small scales, the four expressions for third-order structure function with different normalizations, Eqs. (5)–(8), become

$$\langle\Delta u^3\rangle = u_\tau^3\tilde{\phi}_1\left(\frac{r}{z}\right) = -\frac{4}{5}\epsilon r\left(\tilde{C}_1\frac{u_\tau^3}{\epsilon z}\right) = -\frac{4}{5}\epsilon r\left(\tilde{C}_1\frac{\kappa P}{\epsilon}\right), \tag{14a}$$

$$\langle\Delta u^3\rangle = u_\tau^3\tilde{\phi}_2\left(\frac{\epsilon r}{u_\tau^3}\right) = -\frac{4}{5}\epsilon r\tilde{C}_2, \tag{14b}$$

$$\langle\Delta u^3\rangle = \epsilon z\tilde{\phi}_3\left(\frac{r}{z}\right) = -\frac{4}{5}\epsilon r\tilde{C}_3, \tag{14c}$$

$$\langle\Delta u^3\rangle = \epsilon z\tilde{\phi}_4\left(\frac{\epsilon r}{u_\tau^3}\right) = -\frac{4}{5}\epsilon r\left(\tilde{C}_4\frac{\epsilon z}{u_\tau^3}\right) = -\frac{4}{5}\epsilon r\left(\tilde{C}_4\frac{\epsilon}{\kappa P}\right), \tag{14d}$$

where $\tilde{C}_2 = \tilde{C}_3 = 1$, $\tilde{C}_1$ and $\tilde{C}_4$ are constants to make the quantity in parentheses of the last equality equal to 1, and the derivation above uses $P \approx u_\tau^3/(\kappa z)$. Thus, to be consistent with small Kolmogorov scale, the dimensionless functions $\tilde{\phi}_1$ and $\tilde{\phi}_4$ can be applied only in the case of $\epsilon \sim 1/z$ and, if the mean velocity profile is logarithmic, a z-invariant P/ϵ; otherwise, $\tilde{C}_1$ or $\tilde{C}_4$ would be a z-dependent constant. Also each expression in Eq. (14) captures a combination of power and logarithmic regimes and the two regimes match at a transition scale. Thus we expect that, if P/ϵ does not change remarkably with z, P/ϵ only modifies the expressions through changing the transition scale, and that Eqs. (14b) and (14c), i.e., Eqs. (6) and (7), have wider ranges of applicability than Eqs. (14a) and (14d), i.e., Eqs. (5) and (8), which we justify below using measured data.

Based on the above discussion, if P/ϵ is approximately a constant which is not equal to unity, we can extend the result of Xie *et al.* [21] [cf. Eq. (13)] to a general form:

$$\langle \Delta u^{+3} \rangle = \tilde{\phi}_1\left(\frac{r}{z}\right) = \begin{cases} -\frac{4}{5\kappa}\frac{r}{z}, & \frac{r_\nu}{z} \ll \frac{r}{z} \leqslant \xi_m, \\ -\frac{4}{5\kappa}\xi_m\left[1 + \ln\left(\frac{r}{z\xi_m}\right)\right], & \xi_m < \frac{r}{z} \ll \frac{\delta}{z}, \end{cases} \tag{15}$$

where the two regimes match at $r_m/z = \xi_m$, where ξ_m can be not equal to 1. Moreover, Davidson and Krogstad [10] stated that, in most shear-dominated boundary layer flows, the ratio of energy production rate and dissipation rate P/ϵ is not always unity, but has a weak dependence on z. They proposed that ϵ actually controls the structure of turbulence rather than z and u_τ^3/ϵ is a more appropriate length scale than z for the structure functions. But using u_τ^3/ϵ instead of z to normalize r does not change the matching procedure to obtain the coefficients in the expressions of structure function. The only difference is that the matching location $r_m/z = \xi_m$ is replaced by $\epsilon r_m/u_\tau^3 = \xi_m'$. Thus, repeating the same procedure of getting Eq. (15), we obtain

$$\langle \Delta u^{+3} \rangle = \tilde{\phi}_2\left(\frac{\epsilon r}{u_\tau^3}\right) = \begin{cases} -\frac{4}{5}\frac{\epsilon r}{u_\tau^3}, & \frac{\epsilon r_\nu}{u_\tau^3} \ll \frac{\epsilon r}{u_\tau^3} \leqslant \xi_m', \\ -\frac{4}{5}\xi_m'\left[1 + \ln\left(\frac{\epsilon r}{u_\tau^3 \xi_m'}\right)\right], & \xi_m' < \frac{\epsilon r}{u_\tau^3} \ll \frac{\epsilon\delta}{u_\tau^3}. \end{cases} \tag{16}$$

Based on the proposal of Davidson and Krogstad [10] and Kolmogorov's theory [cf. Eq. (9)], we imply that the energy flux controls the dynamics; therefore, we propose to use ϵ and z to normalize the third-order structure function:

$$\frac{\langle \Delta u^3 \rangle}{\epsilon z} = \tilde{\phi}_3\left(\frac{r}{z}\right) = \begin{cases} -\frac{4}{5}\frac{r}{z}, & \frac{r_\nu}{z} \ll \frac{r}{z} \leqslant \xi_m, \\ -\frac{4}{5}\xi_m\left[1 + \ln\left(\frac{r}{z\xi_m}\right)\right], & \xi_m < \frac{r}{z} \ll \frac{\delta}{z}. \end{cases} \tag{17}$$

It is worth mentioning that Eq. (16) or Eq. (17) are independent of κ and leave no undetermined constant; therefore, they are perfect expressions to justify the validity of the third-order structure-function theory. As discussed before, Eqs. (16) and (17) are more suitable to analyze ASL data, where the measured quantities such as P/ϵ are sensitive to z. Compared with Eq. (16), in Eq. (17) u_τ is removed from the expression since its value can be set by the combination of ϵ and z. Furthermore, u_τ is a quantity that is difficult to determine in ASL flow, because the measured Reynolds stress $\langle uw \rangle$ always varies with z [25]. Let alone in sand-laden flows u_τ is troublesome to define since the sand and dust particles are not uniform in height z, so the absence of u_τ in Eq. (17) is practically helpful. Based on the above considerations we choose Eq. (7) as the normalization method for $\langle \Delta u^3 \rangle$. Comparisons with other normalization methods in Eqs. (5), (6), and (8) are discussed in the Appendix.

Under the assumption of the combined form of Kolmogorov and logarithmic scalings and without an intermediate regime, we can propose a global expression for the third-order structure function with a matching point ξ_m or ξ_m' [cf. Eqs. (15), (16), and (17)]. The change of ξ_m reflects the modification of the range of inertial and logarithmic regimes, which is influenced by the ratio of energy production and dissipation rate P/ϵ. Also for the case of a z-dependent P/ϵ, expression Eq. (17) is capable of normalizing the structure functions with different heights with the same ξ_m, which results in

$$\frac{\langle \Delta u^3 \rangle}{\epsilon z \xi_m} = \begin{cases} -\frac{4}{5}\frac{r}{z\xi_m}, & \frac{r_\nu}{z\xi_m} \ll \frac{r}{z\xi_m} \leqslant 1, \\ -\frac{4}{5}\left[1 + \ln\left(\frac{r}{z\xi_m}\right)\right], & 1 < \frac{r}{z\xi_m} \ll \frac{\delta}{z\xi_m}. \end{cases} \tag{18}$$

This expression contains no other undetermined parameters and is suitable to contradistinguish different flows. Throughout the remainder of the article, we justify the theory of third-order structure function and use Eqs. (17) and (18) to analyze ASL data with and without sand.

III. DETAILS OF ASL DATA

A. Experimental facility

The ASL data used in this work come from the QLOA site, which is located on the flat dry lake bed of Qingtu Lake between the Badain Jaran Desert and the Tenger Desert in western China (E: 103°40′03″, N: 39°12′27″). The observation array consists of 21 towers, with the main tower 32 m high and the other 20 lower towers 5 m high, which can synchronously measure three components of wind velocities and dust concentrations. The panorama and schematic diagram of QLOA can be found in Wang and Zheng [25] and Wang *et al.* [36]. Eleven three-component sonic anemometers (Campbell scientific, CSAT-3B) with a sampling frequency of 50 Hz were installed on the main tower at heights from 0.9 to 30 m to measure wind velocity and temperature. And 20 anemometers of the same type were installed on lower towers at 5 m. The anemometer's wind speed measurement range is 0 to 45 m s^{-1}, with a minimum resolution of 0.01 m s^{-1} and less than 1% relative error (root mean squared). The wind direction records range from 0 to 359°, with a minimum resolution of 1° and less than 1° absolute error. The temperature measurement range is from −40 to 60 °C, with a minimum resolution of 1 °C and less than 1 °C absolute error. At the same height as the sonic anemometers on the main tower, 11 aerosol monitors (TSI, DUSTTRAK II-8530-EP) were installed to measure PM10 (particulate matter with size below 10 μm) concentrations. In field measurements the measuring range of aerosol monitors was set as 0–40 mg m^{-3}. Two sand particle counters measuring the sand saltation fluxes near the surface were installed at 0.2 m and 0.3 m on the main tower, but we analyze higher altitudes and only the influence of dust concentration is considered. The sonic anemometers and aerosol monitors were all connected to data acquisition instruments that were time synchronized with the global positioning system.

B. Data pretreatment

The long-time variability of atmospheric turbulence makes it necessary to select and preprocess the raw data. The same data selection and pretreatment methods as previous studies on ASL measurements [24,25] are implemented to obtain statistically stationary and near-neutral data. The raw velocity data are divided into hourly time series, and then the pretreatments including stratification stability judgment, wind direction adjustment, detrending manipulation, and steady wind selection are carried out.

In field measurements, the temperature of ASL varies throughout the day, due to sunrise and sunset and other weather events, and the temperature variation affects the budget of turbulent kinetic energy in atmospheric turbulence [51]. To characterize the ratio of the buoyancy and shear effects, we consider the Monin-Obukhov stratification parameter [52]

$$\frac{z}{L} = -\frac{\kappa z g \langle w\theta\rangle}{\langle\theta\rangle u_\tau^3}, \tag{19}$$

where z is the distance to the bottom boundary, L is the Obukhov length [53], g is the acceleration of gravity, and $\langle w\theta\rangle$ is the mean vertical heat flux calculated by averaging the covariance of the vertical wind velocity w and the temperature θ. When $|z/L| \ll 1$, the impact of density stratification can be neglected and the shear-dominated ASL flow is near neutral. In our analysis, the Monin-Obukhov stability parameter z/L is obtained at $z = 1.71$ m and it satisfies $|z/L| < 0.06$, which is consistent with near neutrality.

Although the streamwise direction of the observation array is in accord with the prevailing wind direction, the wind direction always changes during field measurements, so the raw data need to be adjusted according to the angle α between the actual wind direction and the streamwise direction of the observation array, i.e.,

$$u = u_m \cos\alpha + v_m \sin\alpha, \quad v = v_m \cos\alpha - u_m \sin\alpha, \tag{20}$$

TABLE I. Main information of the selected clear-air ASL measurement data.

No.	Time and date	State	u_τ (m s^{-1})	Re$_\tau$ ($\times 10^6$)	ν ($\times 10^{-5}$ m^{2}s^{-1})	z/L ($\times 10^{-3}$)	γ (%)
1	04:00–05:00, May 10, 2015	Clear air	0.46	4.94	1.41	3.40	6.12
2	05:00–06:00, May 10, 2015	Clear air	0.51	5.49	1.40	2.36	7.50
3	07:00–08:00, May 10, 2015	Clear air	0.51	5.46	1.41	8.75	11.06
4	15:00–16:00, May 14, 2015	Clear air	0.46	4.45	1.55	-44.33	17.48
5	17:00–18:00, May 14, 2015	Clear air	0.46	4.44	1.55	-28.84	25.28
6	16:00–17:00, May 27, 2015	Clear air	0.39	3.82	1.55	-14.33	7.87
7	19:00–20:00, May 27, 2015	Clear air	0.52	5.20	1.50	-1.29	5.31
8	02:00–03:00, May 29, 2015	Clear air	0.37	3.78	1.49	9.96	2.47
9	04:00–05:00, May 29, 2015	Clear air	0.39	3.98	1.48	6.70	16.05
10	08:00–09:00, May 29, 2015	Clear air	0.30	3.08	1.48	-18.50	26.41

where u_m and v_m are the streamwise and spanwise velocities measured by the anemometers and u and v are the adjusted actual streamwise and spanwise velocities.

In addition, long-term synoptic waves are filtered out through a low-pass filter with a cutoff wavelength of 20δ to extract turbulence fluctuations. From the turbulent velocity data obtained through the above processing, the statistically stationary data should be selected for subsequent analysis. The nonstationary index γ is calculated as

$$\gamma = |(\sigma_\mathrm{m} - \sigma_\mathrm{I})/\sigma_\mathrm{I}| \times 100\%, \tag{21}$$

where $\sigma_\mathrm{m} = \sum_{i=1}^{12} \sigma_i/12$, $\sigma_1, \sigma_2, \ldots, \sigma_{12}$ are the streamwise velocity variances of one-twelfth part of the entire time interval and σ_I is the overall variance of the time interval. High-quality data with $\gamma < 30\%$ are selected, and the above judgment method of near-neutral and steady wind conditions is the same as the previous analysis of QLOA data, as detailed in Wang and Zheng [25] and Wang *et al.* [36].

In this work, we select 20 time intervals of clear-air and sand-containing data described with key features in Tables I and II, respectively. Due to the deviation of the odd-order moments of velocity data, in order to obtain a more convergent third-order structure function, the data used in the calculation is half an hour of the time intervals. These data sets are statistically steady and near neutral with Reynolds numbers Re$_\tau = O(10^6)$. To study the law of wall, we need the value of u_τ, which, however, is not directly measured in ASL experiments. An alternative is to use the relation $u_\tau \approx (-\langle uw \rangle)^{1/2}$ [5,24,54,55], but in ASL measurements $\langle uw \rangle$ are usually height dependent even in the range with logarithmic mean-velocity profile [25]. So, when estimating u_τ, some researchers

TABLE II. Main information of the selected sand-laden ASL measurement data.

No.	Time and date	State	u_τ (m s^{-1})	Re$_\tau$ ($\times 10^6$)	ν ($\times 10^{-5}$ m^{2}s^{-1})	z/L ($\times 10^{-3}$)	γ (%)
1	19:00–20:00, Apr 17, 2015	Sand laden	0.61	6.22	1.47	1.41	7.73
2	09:00–10:00, Mar 18, 2016	Sand laden	0.39	4.12	1.41	-11.84	20.78
3	16:00–17:00, Mar 18, 2016	Sand laden	0.46	4.55	1.51	-22.03	10.69
4	08:00–09:00, Apr 11, 2016	Sand laden	0.45	4.68	1.46	2.94	10.39
5	09:00–10:00, Apr 11, 2016	Sand laden	0.50	5.13	1.47	-8.25	7.95
6	10:00–11:00, Apr 11, 2016	Sand laden	0.56	5.67	1.47	-10.09	20.30
7	08:00–09:00, May 14, 2016	Sand laden	0.55	5.76	1.45	-12.78	7.12
8	14:00–15:00, Mar 27, 2017	Sand laden	0.50	5.13	1.46	-29.66	23.30
9	08:00–09:00, Apr 17, 2017	Sand laden	0.44	4.54	1.46	-6.99	6.39
10	19:00–20:00, Apr 17, 2017	Sand laden	0.31	3.12	1.47	24.82	18.04

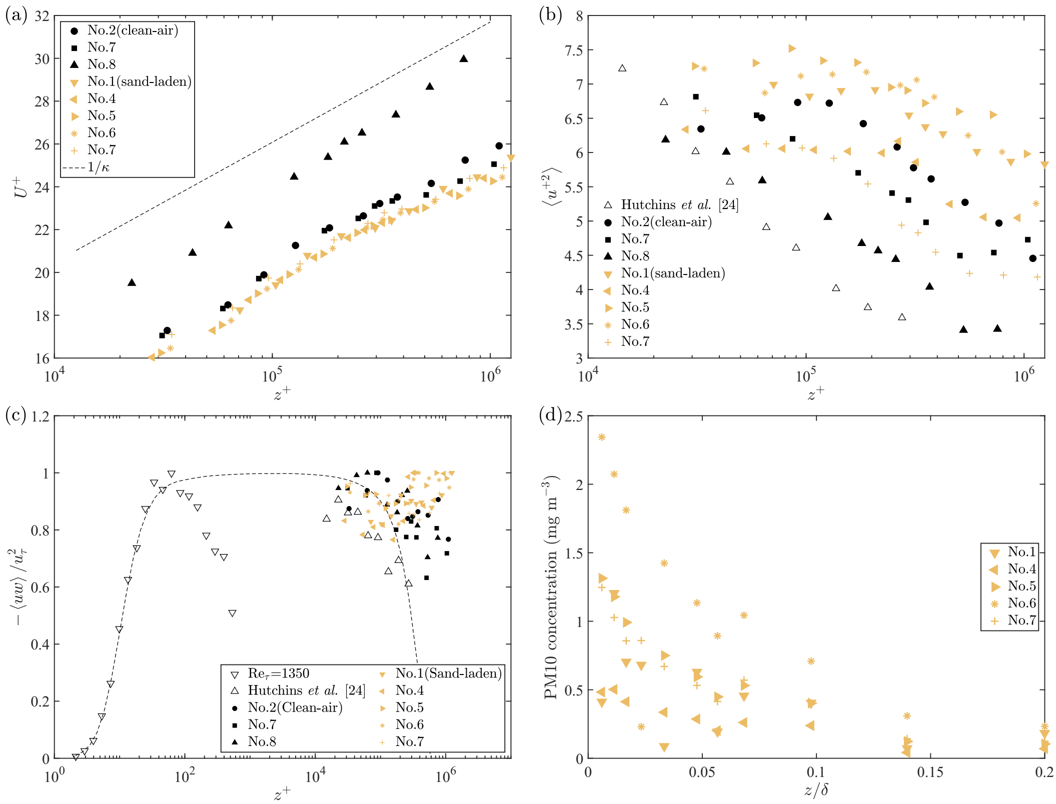

FIG. 1. Some basic flow information of the selected intervals at $\mathrm{Re}_\tau = O(10^6)$. (a) The streamwise mean velocity profile. The solid symbol is the ASL measurement from QLOA and the dashed line corresponds to the slope of $\kappa = 0.41$. (b) The second moments for fluctuating velocity. The open down-pointed triangular is the ASL result of Hutchins *et al.* [24] at $\mathrm{Re}_\tau = O(10^6)$. (c) The shear Reynolds stress. The open up-pointed triangular is the wind tunnel result of de Graaff and Eaton [56] at $\mathrm{Re}_\tau = 1350$ and the dashed line is the similarity formulation from Chauhan [55]. (d) The concentration of PM10 in the sand-laden ASL flow.

use the height averaged $-\langle uw \rangle$ [5,54], while others use the peak value of $-\langle uw \rangle$ [24]. de Graaff and Eaton [56] suggested that estimating u_τ from the peak $-\langle uw \rangle$ is inaccurate and will result in a 10% error in u_τ. Considering the possible sand concentration in ASL, estimating u_τ from measured data is more difficult [36]. In Tables I and II the friction velocities are approximated by the maximum value of $(-\langle uw \rangle)^{1/2}$ in the range of measured data. Air kinematic viscosity ν is obtained at a standard atmospheric pressure corresponding to the measured mean temperature. The ASL thickness δ is estimated as 150 m in this study to evaluate the friction Reynolds number Re_τ, which is consistent with previous studies at the QLOA site under the near-neutral stratification conditions [25,36,57].

IV. ANALYZING ASL DATA

In addition to the stationary and near-neutral judgment, the mean velocity profile, the variance of fluctuating velocity, and the Reynolds stress are compared with other ASL measurement and theoretical results of the canonical zero-pressure-gradient turbulent boundary-layer flow, as presented in Fig. 1. In Fig. 1(a), the dimensionless mean streamwise velocity profile shows logarithmic dependence on z^+ both in clean-air and sand-laden ASL flows, with the von Kármán constant $\kappa \approx 0.41$. The turbulent intensities of the streamwise velocity are also log-linear with z^+ and roughly have the same slope as Hutchins *et al.* [24] in Fig. 1(b). In Fig. 1(c) the variation of

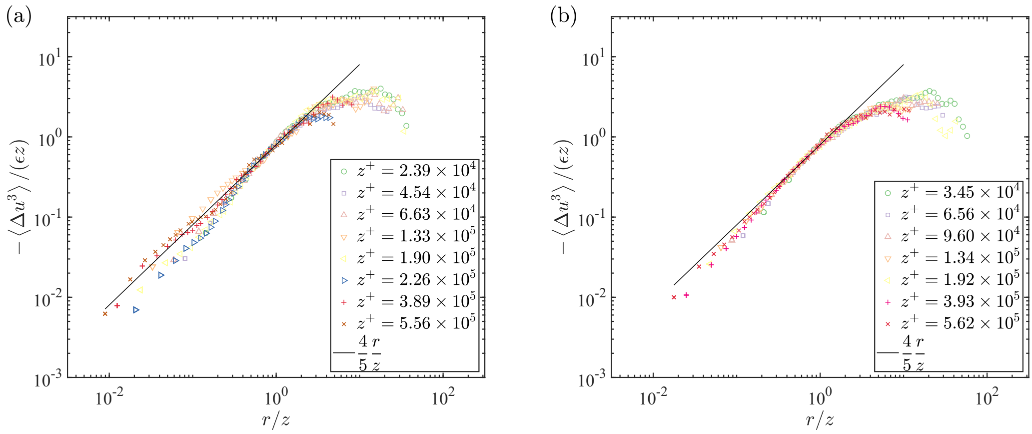

FIG. 2. Log-log plot of the small-scale portions ($r/z \lesssim 1$) of normalized third-order structure function: (a) No. 9 interval for clean-air flow and (b) No. 7 interval for sand-laden flow.

Reynolds stress $\langle uw \rangle$ for clean-air ASL flow shows a trend consistent with the theoretical prediction of Chauhan [55]. Figure 1(d) presents the mean concentration of PM10 in sand-laden flows. The concentration of PM10 decreases with increasing height, which is close to an exponential-decay law [36,58–60].

As shown in 1(c), there exist distinctive behaviors of the vertical momentum flux $\langle uw \rangle$ for clear-air and sand-laden flows. With the presence of sand and dust particles, $-\langle uw \rangle$ increases with height, which can be used to distinguish these two different flows. Besides, other significant differences in sand-laden ASL flow with high Reynolds number have been identified, such as the enhancement of streamwise turbulent kinetic energy [36] and wall-normal turbulence intensity [61], the decrease in velocity gradient, the increase in the inclination angles of the large scale structures, and the amplitude modulation across scales [36,61].

A. Justification of small-scale Kolmogorov scaling

First, we show in Fig. 2 that in the small-scale range ($r/z \lesssim 1$) the third-order structure functions follow Kolmogorov's scaling with linear dependence on r/z. Thanks to the high Reynolds number of ASL, this linear dependence, which is rarely observed in the experimental results or numerical simulations, is justified. And this scaling is checked here in sand-laden ASL flow. Because of the clear linearity of $\langle \Delta u^3 \rangle$ in measured data, to normalize $\langle \Delta u^3 \rangle$ we determine the energy dissipation rate ϵ according to Eq. (9) in this work, which is consistent with previous results saying that estimating ϵ from $\langle \Delta u^3 \rangle$ is more accurate [62,63].

With obtained ϵ we can calculate the ratio between local production and dissipation P/ϵ, which is later used in the study of Eq. (17). Here the local energy production rate is estimated as $P = -\langle uw \rangle dU/dz$. As shown in Fig. 3, in some intervals such as No. 7 for sand-laden flows, P/ϵ is approximately independent of z^+, corresponding to a z-independent transition location ξ_m between the inertial and logarithmic regimes. But in the No. 9 interval for clear-air flows, P/ϵ shows a strong vertical dependence. Data of these two intervals are used to distinguish different normalizations in Eqs. (5)–(8), which are shown in the Appendix.

B. Budgets of KHM equation in the logarithmic region

In this section we check the approximations to the KHM equation in the derivation by Xie *et al.* [21] in the range of $r_m < r \ll \delta$ (r_m/z of the order unity). Here, the existence of $\langle u_1 w_2 + w_1 u_2 \rangle \sim 1/r'$, $\langle |\Delta \mathbf{u}|^2 w_c \rangle \sim 1/r'$ [cf. Eq. (12)] leads to the logarithmic dependence of $\langle \Delta u^3 \rangle$ on r. The terms

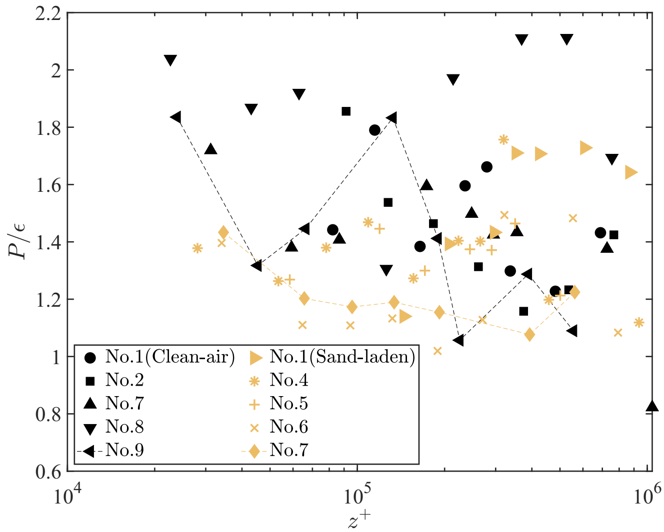

FIG. 3. Height dependence of the ratio between local energy production and dissipation rate P/ϵ of different data sets.

in Eq. (11) are displayed in Fig. 4, from which we can see that, in the selected data, $r'\partial\langle|\Delta\mathbf{u}|^2 w_c\rangle/\partial r'$ is much smaller than the other two terms which form the dominant balance.

Besides, the r^{-1} scaling of $\langle u_1 w_2 + u_2 w_1\rangle$ holds in our ASL data with and without sand, as shown in Fig. 5. $\langle u_1 w_2 + u_2 w_1\rangle$ of different heights are normalized by $\langle uw\rangle$ of the corresponding heights. The r^{-1} scaling holds at $r/z \gtrsim 1$, which is consistent with the empirical result $r_m = z$. In summary, Figs. 2, 4, and 5 justify reduction procedures to the KHM equation and the derivation of logarithmic form of third-order structure function by Xie *et al.* [21].

C. Third-order structure function

Under Taylor's frozen hypothesis [26], which is a common practice in the analysis of streamwise ASL turbulence [24,25,36,64,65], the spatial third-order structure function can be calculated from

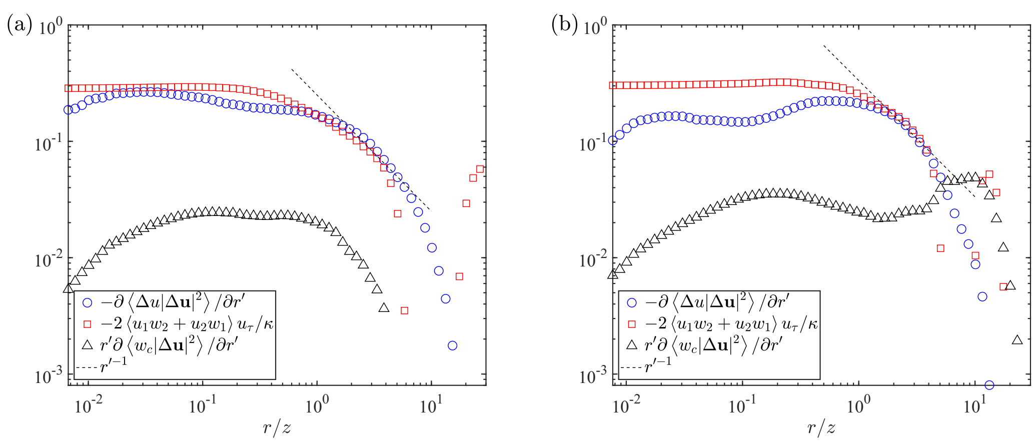

FIG. 4. Energy flux in Eq. (11) (a) at $z^+ \approx 7.65\times10^5$, $\mathrm{Re}_\tau \approx 3.82\times10^6$ for clean-air flow and (b) at $z^+ \approx 6.36\times10^5$, $\mathrm{Re}_\tau \approx 4.55\times10^6$ for sand-laden flow.

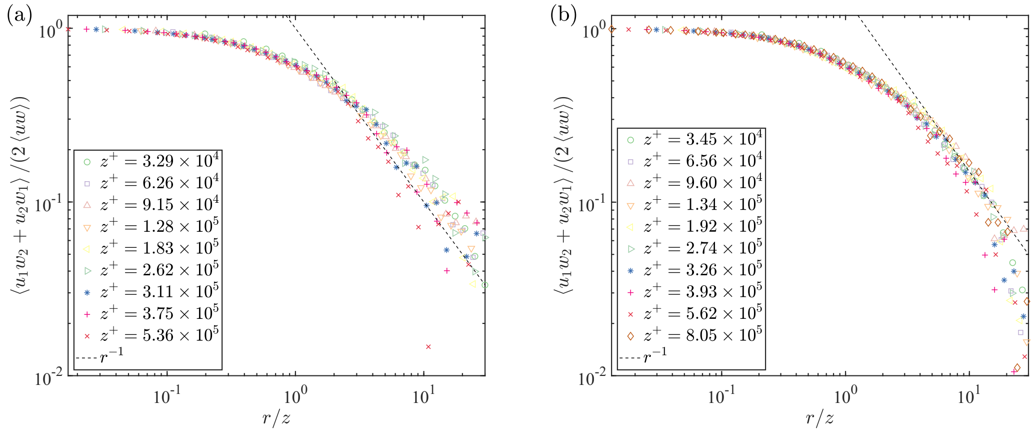

FIG. 5. r^{-1} scaling of $\langle u_1w_2 + u_2w_1 \rangle$ from (a) No. 2 interval for clean-air flow and (b) No. 7 interval for sand-laden flow.

the data measured at fixed positions with different time. As mentioned in Sec. II, for the cases with local production-dissipation balance, the inertial and the logarithmic ranges of the structure functions match at $r/z = O(1)$. In ASL measurement, P/ϵ may vary. We justify the relation Eq. (17) for both clear-air and sand-laden flow. Both panels in Fig. 6 correspond to $P/\epsilon \approx 1.4$ and the matching points ξ_m are found to be of $O(1)$.

In addition, sand-laden data at different heights are also in good agreement with the theoretical curve shown in Fig. 6(b). It indicates that the presence of sand has little effect on the small-scale Kolmogorov's scaling and the logarithmic dependence of the third-order structure function; also, there seems to be no new intermediate regimes between those two regimes as the expressions of the two regimes match at $\xi_m = O(1)$. Though sand has been proved to affect the very large scale motions in ASL and the distribution of kinetic energy across scales [36,61], the behavior of the third-order structure function is still robust and is appropriately described by the expression Eq. (17).

As discussed in Sec. II, there are three other characteristic scale choices besides Eq. (7) for the third-order structure function. The results of applying other normalization methods are shown in the Appendix. Compared with Fig. 6, Figs. 9–11 illustrate that when P/ϵ is z invariant all four

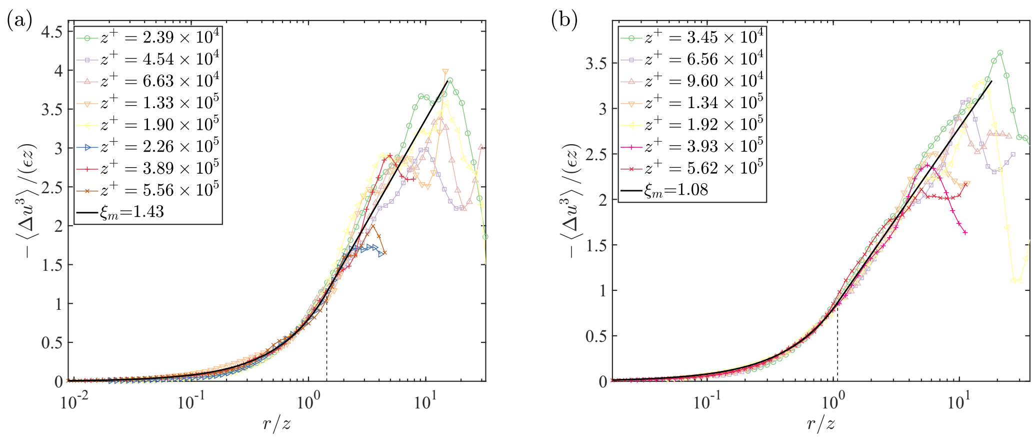

FIG. 6. Normalized third-order structure functions: (a) No. 9 interval for clean-air flow and (b) No. 7 interval for sand-laden flow.

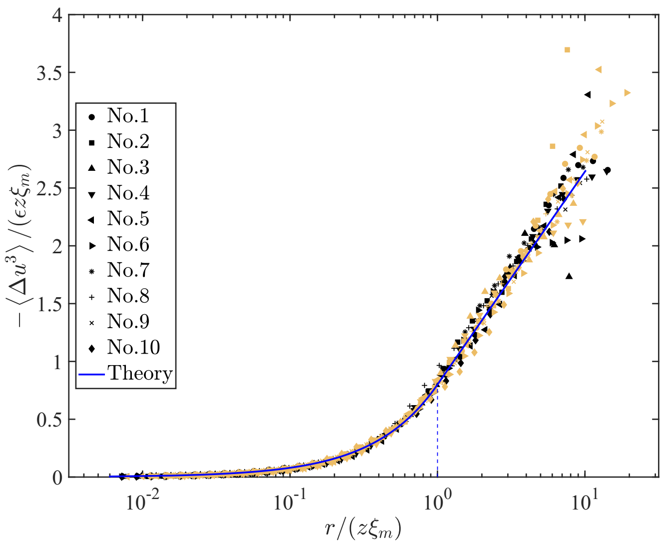

FIG. 7. Comparison between third-order structure functions of all intervals in Tables I and II and the theoretical expression Eq. (18) (blue curve). The same symbol corresponds to the same interval number for clean-air and sand-laden flows and the z^+ range from 1.85×10^4 to 1.04×10^6 for all data sets.

normalizations in Eqs. (5)–(8) work well, while when P/ϵ varies with z Eqs. (5) and (8) are no longer suitable, which is exactly as we expected based on the discussion in Sec. II B.

D. Dependence of matching point ξ_m on P/ϵ

If a universal behavior of $\langle\Delta u^3\rangle$ exists, the normalized results of different data sets should converge to Eq. (18). After taking height average, the results of twenty intervals are demonstrated in Fig. 7. P/ϵ may vary with z in some data sets, but the curves of $\langle\Delta u^3\rangle$ at different heights can be characterized by one matching point ξ_m. Here the results are the average of different heights over the same interval. We find that the structure functions obtained from 20 data sets collapse well, which implies the robustness of our expression Eq. (17) whether ASL flow contains sands or not.

Our theory contains the matching point ξ_m as a important parameter. The variation of ξ_m with P/ϵ is depicted in Fig. 8. Qualitatively, the matching point ξ_m decreases as P/ϵ increases and there is no significant difference between clean-air and sand-laden flows. Though P and ϵ are of the same magnitude, there exists a production-dissipation imbalance. The turbulent transport of kinetic energy makes up for this imbalance, i.e.,

$$P + T = \epsilon, \tag{22}$$

where T is the kinetic energy transferred from other heights to the present height. In the picture of Richardson-Kolmogorov cascade, the energy-containing eddies acquire turbulent kinetic energy from energy production and transfer energy to eddies with smaller sizes. There exists an inertial region in which the energy transfers to the dissipative scale at the rate of ϵ, and the sizes of the vortices in it are much larger than that of the Kolmogorov microscale r_ν and much smaller than that of the energy-containing eddies. The boundary-layer turbulent flow at the large scale is anisotropic but near-isotropic at small scales. The energy production term in the KHM equation $\langle u_1 w_2 + u_2 w_1\rangle dU/dz$ is calculated from the anisotropic Reynolds stress and the anisotropic gradient of mean streamwise velocity; then we can estimate the strength of the anisotropy by the value of $\langle u_1 w_2 + u_2 w_1\rangle dU/dz$ with zero displacement, which is the shear production P, while Kolmogorov's derivation of the third-order structure function's linear dependence on the dissipation

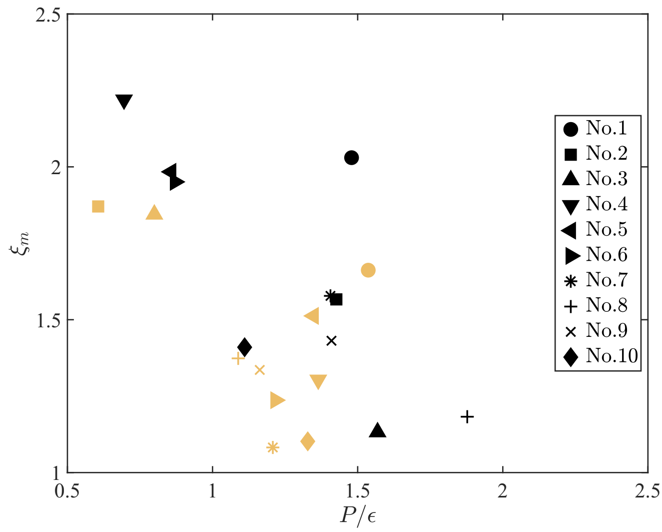

FIG. 8. Matching point ξ_m averaged across heights varies with the ratio of energy production and dissipation rate P/ϵ and the same symbol corresponds to the same interval number for clean-air and sand-laden flows.

rate ϵ bases on the local-isotropic assumption. Thus P/ϵ can be regarded as a parameter measuring the relative strength between anisotropic and isotropic effects and, therefore, we conjecture that, in near-neutral ASL flows, the decrease of P/ϵ results in a wider range for the near-Kolmogorov region and the enlargement of transition scale ξ_m. The above argument is similar to that in the stratified turbulence, where the Kolmogorov turbulence is strengthened by a larger conversion from potential to kinetic energy [66].

V. SUMMARY AND DISCUSSION

By further developing the third-order structure-function theory in boundary-layer turbulence, we analyze the measured data in ASL with and without sand. Our main results are summarized as follows. (i) Using field-measurement data, we check the small-scale Kolmogorov scaling. This result compensates those of de Silva *et al.* [20] for even-order structure functions. (ii) Thanks to the high Reynolds number of ASL data, the dominant balance of the reduced KHM equation derived by Xie *et al.* [21] in ASL turbulence is justified. Thus the logarithmic behavior of the third-order structure function is a result of the balance between energy advection in the streamwise direction and the shear production. (iii) The behavior of a combination of linear and logarithmic dependence on r/z of the third-order structure function is found to be robust by the high-quality clean-air and sand-laden ASL data. Due to the difficulty of determining u_τ in the measured data, expression Eq. (17) where u_τ is absent is the best to show this universal behavior (cf. Fig. 7) and shows less error compared to Eq. (16) when applied on ASL flows, as discussed in the Appendix. (iv) Associated with this universal behavior, we define a parameter ξ_m, which is the transition and matching scale between the power and logarithmic regimes of the third-order structure function. In the ASL flows where the ratio of energy production and dissipation rate P/ϵ does not change dramatically with z, ξ_m decreases as P/ϵ increases, according to the available data. In the perspective of energy transfer across scales, in both the inertial and logarithmic ranges energy transfers to small scales and their major difference is the existence of anisotropic attached eddies in the latter range. Since the shear production is an anisotropic effect, P/ϵ is a natural measure for the relative strength between anisotropic and isotropic effects. So, as the value of P/ϵ increases, the linear Kolmogorov range shrinks and the logarithmic range extends.

The universal behavior of the third-order structure function we obtained shows spatial dependence on r/z. From the perspective of energy flux, we choose the combination of energy dissipation ϵ and the distance to the wall z to normalize third-order structure functions. This scaling is justified by ASL measurements at $\mathrm{Re}_\tau = O(10^6)$. An alternative dependence, u_τ^3/ϵ, was proposed by Davidson and Krogstad [10]. But in our data sets, there is no significant difference between results obtained from these two methods. One advantage of our scaling choice is that it avoids defining friction velocity u_τ in the sand-laden flow where the concentration of PM10 varies with height z. Besides, Davidson and Krogstad [10] proposed new scaling since P/ϵ varies with z. de Silva *et al.* [20] attributed this variation to the finite range of Reynolds number, but here, for $\mathrm{Re}_\tau = O(10^6)$, the variation of P/ϵ with z still appears in field measurements. Our proposals Eqs. (7) and (17), where the velocity is rescaled by characteristic velocity determined by energy dissipation rate, are more suitable for the analysis of ASL measurement data.

Even though we find a universal behavior for ASL with and without sand, this universality may be limited to the sand density in our current data sets. As shown in the last panel of Fig. 1, the concentration of PM10 is at most 2.5 mg m^{-3} and the particles are close to the bottom. It is interesting to further study the situations with more contained sand and different sand containing profiles. Besides the assumptions of our theory including Kolmogorov's small-scale isotropic hypothesis, we invoke the expression of third-order structure function in the inertial subrange. Despite that ASL is not isotropic we still assume the validity of the four-fifths law for the longitudinal structure function, which requires further study.

We close this paper by mentioning some aspects of data measurement that may lead to errors. First, in the ASL measurement, it is hard to find steady boundary-layer turbulence as the environment is always changing. So our data is only restricted to time intervals of half an hour, where the steadiness can be well accepted. Second, the QLOA observation obtains data at different times with the same locations; therefore, we have to use Taylor's frozen hypothesis to obtain spatial structure functions. But the Taylor's frozen hypothesis may not be accurate when dealing with correlation with a long time difference [67] and may impact amplitude modulation [68]. Combined with the limited time interval, the structure functions with large displacement are more inaccurate than those with small displacements, which is hinted at in Figs. 6 and 7. Finally, we prefer neutral boundary layer turbulence to avoid the impact of density stratification, which cannot be strictly guaranteed and further limits our available data sets. In our results, a larger positive transport leads to a wider range of Kolmogorov turbulence, which is similar to the case of stably stratified boundary layer turbulence, where a positive conversion from potential to kinetic energy tends to sustain Kolmogorov turbulence under stronger stable stratification [69]. To describe the effect of temperature, further development of the third-order structure-function theory including buoyancy's impact is required for future study.

ACKNOWLEDGMENTS

We acknowledge valuable discussion with R. Hu, H. Liu, and G. Wang. F.-C.Z. and J.-H.X. gratefully acknowledge the financial support from the National Natural Science Foundation of China (NSFC) under Grant No. 92052102 and Joint Laboratory of Marine Hydrodynamics and Ocean Engineering, Pilot National Laboratory for Marine Science and Technology (Qingdao) under Grant No. 2022QNLM010201. X.Z. gratefully acknowledges financial support from the National Natural Science Foundation of China Grant No. 92052202.

APPENDIX: COMPARISON BETWEEN DIFFERENT CHOICES OF CHARACTERISTIC SCALES IN EQS. (5)–(8)

As discussed in Sec. II B, Eqs. (6) and (7) are more general expressions compared to Eqs. (5) and (8), since the latter two expressions require a z-invariant P/ϵ. We select two representative intervals:

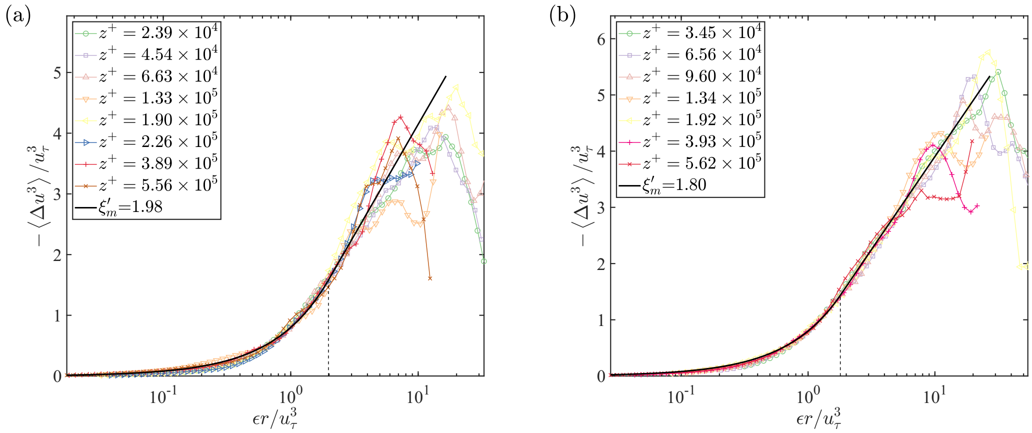

FIG. 9. Third-order structure functions normalized by the scaling of Davidson and Krogstad [10] [cf. Eq. (6)]: (a) No. 9 interval for clean-air flow and (b) No. 7 interval for sand-laden flow.

No. 9 for clean-air flows and No. 7 for sand-laden flows (note by No. 9 and No. 7 for simplicity). The variations of P/ϵ with z in No. 9 and No. 7 are dotted in Fig. 2. In No. 9 P/ϵ is more discrete with z and in No. 7 P/ϵ is approximately z independent.

For the case that P/ϵ varies with z, Davidson and Krogstad [10] proposed the spatial scale z should be replaced by u_τ^3/ϵ. Compared with Fig. 6, the normalization results of Davidson and Krogstad [10] shown in Fig. 9 are similar to our proposal, except that the matching point ξ'_m is transformed. The maximum value of $(-\langle uw \rangle)^{1/2}$ is used in this section to approximate u_τ (cf. Tables I and II). There is no significant diversity in the collapsing of data using Eqs. (16) and (17), which is expected in our theory. The two normalization methods Eqs. (6) and (7) have no essential difference, since for the small-scale isotropic regime the two expressions are the same and a matching point exists to connect with the logarithmic regime. The other two normalization methods Eqs. (5) and (8) are in sharp contrast in the left and right panels of Figs. 10 and 11. Only Eqs. (6) and (7) can normalize $\langle \Delta u^3 \rangle$ of different heights in No. 9, since P/ϵ shows dependence on z. All four normalizations in Eqs. (5)–(8) work well for No. 7, as shown in the right panel of Figs. 6, 9–11. Further, between Eqs. (6) and (7) we choose Eq. (7). Though the two expressions are the same in the small-scale inertial regime, Eq. (6) causes errors at large-scale logarithmic regime due to the

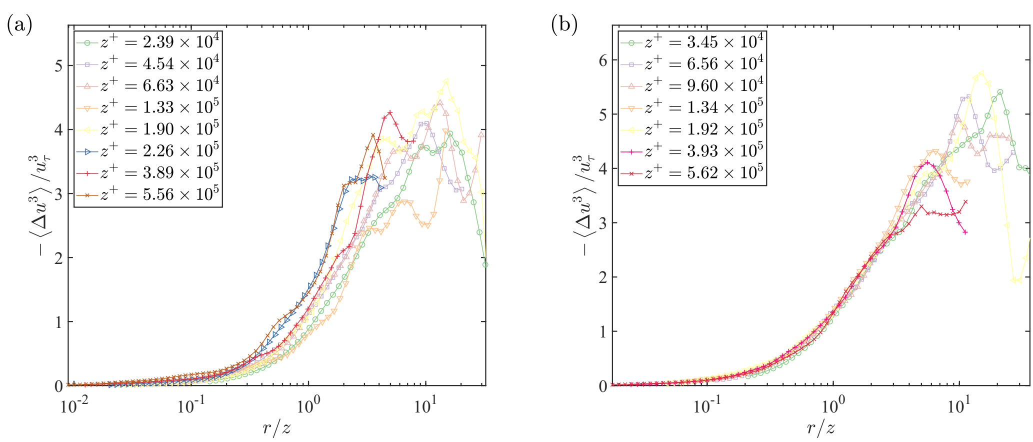

FIG. 10. Analysis using Eq. (5) of same intervals in Fig. 9.

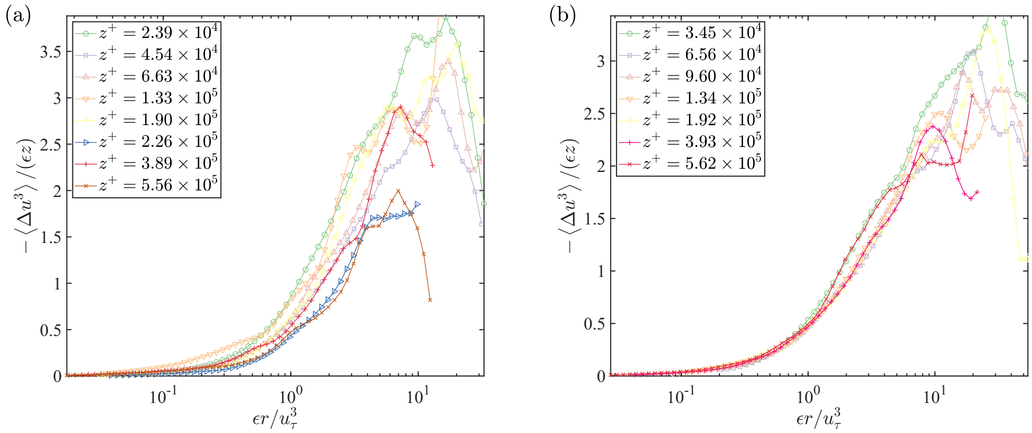

FIG. 11. Analysis using Eq. (8) of same intervals in Fig. 9.

measured data. In Eqs. (17) and (16), the slope of the logarithmic regime is determined by ξ_m or ξ_m', which is height dependent. So we use the mean values of ξ_m or ξ_m' as characteristics, and apply the mean absolute percentage error (MAPE) to judge the accuracy in each interval. In both the clear-air and sand-laden ASL flows, the MAPE of ξ_m' is larger than those of ξ_m, implying that Eq. (17) is better applicable to real data and we think this difference mainly comes from the estimation of u_τ in Eq. (16). As such, the logarithmic expression of Eq. (6) can be written as

$$\begin{aligned} \langle \Delta u^{+3} \rangle &= \tilde{D}_3 \ln\left(\frac{\epsilon r}{u_\tau^3}\right) + \tilde{B}_3 \\ &= \tilde{D}_3 \ln\left(\frac{r}{z}\right) + \tilde{D}_3 \ln\left(\frac{\epsilon z}{u_\tau^3}\right) + \tilde{B}_3 \\ &= \tilde{D}_3 \ln\left(\frac{r}{z}\right) + \tilde{D}_3 \ln\left(\frac{\epsilon}{\kappa P}\right) + \tilde{D}_3 \ln\left(\frac{-\langle uw \rangle}{u_\tau^2}\right) + \tilde{B}_3, \end{aligned} \tag{A1}$$

where $\tilde{D}_3$ and $\tilde{B}_3$ are constants. The local energy production rate P is estimated as $-\langle uw \rangle dU/dz$, but in field measurements $\langle uw \rangle$ is sensitive to z [25]. So when applying the scaling of Davidson and Krogstad [10] on data analysis, error arises due to the deviation between $-\langle uw \rangle$ and u_τ^2. In some cases, such as sand-laden ASL flow, how to define u_τ is already a dilemma, not to mention the error caused by the calculation of u_τ. Given all this, we adopt Eqs. (7) and (17) in our study.

[1] S. B. Pope, *Turbulent Flows* (Cambridge University Press, Cambridge, UK, 2001).
[2] L. Prandtl, Bericht über Untersuchungen zur ausgebildeten turbulenz, Z. Angew. Math. Mech. **5**, 136 (1925).
[3] T. von Kármán, Mechanische Aehnlichkeit und Turbulenz, in *Proceedings of the Third International Congress of Applied Mechanics* (P. A. Norstedt & Soner, Stockholm, 1930), Vol. 1, pp. 85–105.
[4] A. A. R. Townsend, *The Structure of Turbulent Shear Flow*, (Cambridge University Press, Cambridge, UK, 1976), Vol. 727, p. 155.
[5] I. Marusic, J. P. Monty, M. Hultmark, and A. J. Smits, On the logarithmic region in wall turbulence, J. Fluid Mech. **716**, R3 (2013).
[6] Y. Yamamoto and Y. Tsuji, Numerical evidence of logarithmic regions in channel flow at $\mathrm{Re}_\tau = 8000$, Phys. Rev. Fluids **3**, 012602(R) (2018).
[7] H. H. A. Xu and X. I. A. Yang, Fractality and the law of the wall, Phys. Rev. E **97**, 053110 (2018).

[8] D. C. Wilcox, *Turbulence Modeling for CFD* (DCW Industries, La Canada, CA, 1998).
[9] C. Meneveau and I. Marusic, Generalized logarithmic law for high-order moments in turbulent boundary layers, J. Fluid Mech. **719**, R1 (2013).
[10] P. A. Davidson and P.-Å. Krogstad, A universal scaling for low-order structure functions in the log-law region of smooth- and rough-wall boundary layers, J. Fluid Mech. **752**, 140 (2014).
[11] J. D. Woodcock and I. Marusic, The statistical behaviour of attached eddies, Phys. Fluids **27**, 015104 (2015).
[12] A. N. Kolmogorov, Dissipation of energy in the locally isotropic turbulence, Dokl. Akad. Nauk SSSR A **32**, 16 (1941).
[13] R. J. Hill, Exact second-order structure-function relationships, J. Fluid Mech. **468**, 317 (2002).
[14] J. M. Vindel, C. Yagüe, and J. M. Redondo, Structure function analysis and intermittency in the atmospheric boundary layer, Nonlin. Processes Geophys. **15**, 915 (2008).
[15] J.-H. Xie and O. Bühler, Third-order structure functions for isotropic turbulence with bidirectional energy transfer, J. Fluid Mech. **877**, R3 (2019).
[16] I. Marusic and J. P. Monty, Attached eddy model of wall turbulence, Annu. Rev. Fluid Mech. **51**, 49 (2019).
[17] P. A. Davidson, T. B. Nickels, and P.-Å. Krogstad, The logarithmic structure function law in wall-layer turbulence, J. Fluid Mech. **550**, 51 (2006).
[18] P. A. Davidson, P.-Å. Krogstad, and T. B. Nickels, A refined interpretation of the logarithmic structure function law in wall layer turbulence, Phys. Fluids **18**, 065112 (2006).
[19] P. A. Davidson and P.-Å. Krogstad, A simple model for the streamwise fluctuations in the log-law region of a boundary layer, Phys. Fluids **21**, 055105 (2009).
[20] C. M. de Silva, I. Marusic, J. D. Woodcock, and C. Meneveau, Scaling of second- and higher-order structure functions in turbulent boundary layers, J. Fluid Mech. **769**, 654 (2015).
[21] J.-H. Xie, C. de Silva, R. Baidya, X. I. A. Yang, and R. Hu, Third-order structure function in the logarithmic layer of boundary-layer turbulence, Phys. Rev. Fluids **6**, 074602 (2021).
[22] X. I. A. Yang, R. Baidya, P. Johnson, I. Marusic, and C. Meneveau, Structure function tensor scaling in the logarithmic region derived from the attached eddy model of wall-bounded turbulent flows, Phys. Rev. Fluids **2**, 064602 (2017).
[23] G. J. Kunkel and I. Marusic, Study of the near-wall-turbulent region of the high-Reynolds-number boundary layer using an atmospheric flow, J. Fluid Mech. **548**, 375 (2006).
[24] N. Hutchins, K. Chauhan, I. Marusic, J. Monty, and J. Klewicki, Towards reconciling the large-scale structure of turbulent boundary layers in the atmosphere and laboratory, Boundary-Layer Meteorol. **145**, 273 (2012).
[25] G. Wang and X. Zheng, Very large scale motions in the atmospheric surface layer: a field investigation, J. Fluid Mech. **802**, 464 (2016).
[26] G. I. Taylor, The spectrum of turbulence, Proc. R. Soc. London A **164**, 476 (1938).
[27] G. Hetsroni, Particles-turbulence interaction, Int. J. Multiphase Flow **15**, 735 (1989).
[28] J. D. Kulick, J. R. Fessler, and J. K. Eaton, Particle response and turbulence modification in fully developed channel flow, J. Fluid Mech. **277**, 109 (1994).
[29] L. H. Zhao, H. I. Andersson, and J. J. J. Gillissen, Turbulence modulation and drag reduction by spherical particles, Phys. Fluids **22**, 081702 (2010).
[30] G. F. K. Tay, D. C. S. Kuhn, and M. F. Tachie, Effects of sedimenting particles on the turbulence structure in a horizontal channel flow, Phys. Fluids **27**, 025106 (2015).
[31] Y. Tsuji and Y. Morikawa, LDV measurements of an air-solid two-phase flow in a horizontal pipe, J. Fluid Mech. **120**, 385 (1982).
[32] Y. Tsuji, Y. Morikawa, and H. Shiomi, LDV measurements of an air-solid two-phase flow in a vertical pipe, J. Fluid Mech. **139**, 417 (1984).
[33] X. Zheng, J. Zhang, G. Wang, H. Liu, and W. Zhu, Investigation on very large scale motions (VLSMs) and their influence in a dust storm, Sci. China Phys. Mech. Astron. **56**, 306 (2013).
[34] G. Wang, X. Zheng, and J. Tao, Very large scale motions and PM10 concentration in a high-Re boundary layer, Phys. Fluids **29**, 061701 (2017).

[35] Y. Zhang, R. Hu, and X. Zheng, Large-scale coherent structures of suspended dust concentration in the neutral atmospheric surface layer: A large-eddy simulation study, Phys. Fluids **30**, 046601 (2018).
[36] G. Wang, H. Gu, and X. Zheng, Large scale structures of turbulent flows in the atmospheric surface layer with and without sand, Phys. Fluids **32**, 106604 (2020).
[37] H. A. Einstein and N. Chien, *Effect of Heavy Sediment Concentration Near the Bed on Velocity and Sediment Distribution* (University of California, Berkeley, CA, 1955), Vol. 33, p. 2.
[38] D. A. Lyn, Ph.D. thesis, California Institute of Technology, 1986.
[39] D. A. Lyn, A similarity approach to turbulent sediment-laden flows in open channels, J. Fluid Mech. **193**, 1 (1988).
[40] J. Guo and P. Y. Julien, Turbulent velocity profiles in sediment-laden flows, J. Hydraul. Res. **39**, 11 (2001).
[41] O. Castro-Orgaz, J. V. Giráldez, L. Mateos, and S. Dey, Is the von Kármán constant affected by sediment suspension?, J. Geophys. Res. **117** (2012).
[42] N. L. Coleman, Velocity profiles with suspended sediment, J. Hydraul. Res. **19**, 211 (1981).
[43] N. L. Coleman, Effects of suspended sediment on the open-channel velocity distribution, Water Resour. Res. **22**, 1377 (1986).
[44] G. Parker and N. L. Coleman, Simple model of sediment-laden flows, J. Hydraul. Eng. **112**, 356 (1986).
[45] L. F. Janin and J. E. Cermak, Sediment-laden velocity profiles developed in a long boundary-layer wind tunnel, J. Wind Eng. Ind. Aerodyn. **28**, 159 (1988).
[46] F. Cioffi and F. Gallerano, Velocity and concentration profiles of solid particles in a channel with movable and erodible bed, J. Hydraul. Res. **29**, 387 (1991).
[47] I. Marusic and N. Hutchins, Study of the log-layer structure in wall turbulence over a very large range of Reynolds number, Flow. Turbul. Combust. **81**, 115 (2008).
[48] T. Wei, Integral properties of turbulent-kinetic-energy production and dissipation in turbulent wall-bounded flows, J. Fluid Mech. **854**, 449 (2018).
[49] M. Metzger, B. J. McKeon, and H. Holmes, The near-neutral atmospheric surface layer: turbulence and non-stationarity, Philos. Trans. R. Soc. London A **365**, 859 (2007).
[50] H. Tennekes and J. L. Lumley, *A First Course in Turbulence* (MIT Press, Cambridge, MA, 2018).
[51] J. C. Wyngaard and O. R. Coté, The budgets of turbulent kinetic energy and temperature variance in the atmospheric surface layer, J. Atmos. Sci. **28**, 190 (1971).
[52] A. S. Monin and A. M. Obukhov, Basic laws of turbulentmixing in the atmospheric surface layer, Tr. Akad. Nauk SSSR Geofiz. Insti. **24**, 163 (1954).
[53] A. M. Obukhov, Turbulence in thermally inhomogeneous atmosphere, Trudy Inst. Teor. Geofiz. Akad. Nauk SSSR **1**, 95 (1946).
[54] U. L. F. Högström, Von Karman's constant in atmospheric boundary layer flow: Reevaluated, J. Atmos. Sci. **42**, 263 (1985).
[55] K. A. Chauhan, Ph.D. thesis, Illinois Institute of Technology, 2007.
[56] D. B. de Graaff and J. K. Eaton, Reynolds-number scaling of the flat-plate turbulent boundary layer, J. Fluid Mech. **422**, 319 (2000).
[57] H. Liu, T. Bo, and Y. Liang, The variation of large-scale structure inclination angles in high Reynolds number atmospheric surface layers, Phys. Fluids **29**, 035104 (2017).
[58] H. A. McGowan and A. Clark, A vertical profile of PM10 dust concentrations measured during a regional dust event identified by MODIS Terra, western Queensland, Australia, J. Geophys. Res.: Solid Earth **113**, F02S03(2008).
[59] J. E. Panebianco, D. E. Buschiazzo, and T. M. Zobeck, Comparison of different mass transport calculation methods for wind erosion quantification purposes, Earth Surf. Processes Landforms **35**, 1548 (2010).
[60] J. E. Panebianco, M. J. Mendez, and D. E. Buschiazzo, PM10 emission, sandblasting efficiency and vertical entrainment during successive wind-erosion events: a wind-tunnel approach, Boundary-Layer Meteorol. **161**, 335 (2016).
[61] H. Liu, X. He, and X. Zheng, An investigation of particles effects on wall-normal velocity fluctuations in sand-laden atmospheric surface layer flows, Phys. Fluids **33**, 103309 (2021).
[62] J. D. Albertson, M. B. Parlange, G. Kiely, and W. E. Eichinger, The average dissipation rate of turbulent kinetic energy in the neutral and unstable atmospheric surface layer, J. Geophys. Res. **102**, 13423 (1997).

[63] K. R. Sreenivasan and R. A. Antonia, The phenomenology of small-scale turbulence, Annu. Rev. Fluid Mech. **29**, 435 (1997).

[64] N. Hutchins and I. Marusic, Evidence of very long meandering features in the logarithmic region of turbulent boundary layers, J. Fluid Mech. **579**, 1 (2007).

[65] H. Y. Liu, G. H. Wang, and X. J. Zheng, Spatial length scales of large-scale structures in atmospheric surface layers, Phys. Rev. Fluids **2**, 064606 (2017).

[66] M. K. Verma, A. Kumar, and A. Pandey, Phenomenology of buoyancy-driven turbulence: recent results, New J. Phys. **19**, 025012 (2017).

[67] G. He, G. Jin, and Y. Yang, Space-time correlations and dynamic coupling in turbulent flows, Annu. Rev. Fluid Mech. **49**, 51 (2017).

[68] X. I. A. Yang and M. F. Howland, Implication of Taylor's hypothesis on measuring flow modulation, J. Fluid Mech. **836**, 222 (2018).

[69] L. S. Freire, M. Chamecki, E. Bou-Zeid, and N. L. Dias, Critical flux Richardson number for Kolmogorov turbulence enabled by TKE transport, Quart. J. Roy. Meteor. Soc. **145**, 1551 (2019).